Research Article Vol. 3, No. 6 / June 2016 / Optica 592

Planar metal/dielectric single-periodic multilayer ultraviolet flat lens

Ruben Maas,[1] Jorik van de Groep,[1,2] and Albert Polman[1,*]

[1]Center for Nanophotonics, FOM Institute AMOLF, Science Park 104, 1098 XG Amsterdam, The Netherlands
[2]Currently at Geballe Laboratory for Advanced Materials, Stanford University, 476 Lomita Mall, Stanford, California 94305, USA
*Corresponding author: polman@amolf.nl

Received 29 December 2015; revised 29 March 2016; accepted 29 April 2016 (Doc. ID 255811); published 7 June 2016

In 1968, Veselago predicted that a thin film composed of a material with a negative refractive index would act as a flat lens [Sov. Phys. Usp. 10, 509 (1968)]. Hyperbolic metamaterials have been designed that show negative refraction, but the condition of an isotropic refractive index $n = -1$ required to realize a diffraction-limited focus cannot be realized using the hyperbolic dispersion. Here, we present an experimental realization of a metamaterial design in which the dispersion is described by spherical rather than hyperbolic isofrequency wavevector contours, emulating an isotropic refractive index $n = -1$. We fabricate a flat lens that operates in the UV at $\lambda = 364$ nm using a silver/titanium dioxide single-periodic thin-film multilayer structure. Using confocal microscopy, we find a clear focus positioned only 350 nm away from the flat lens surface, in very good agreement with analytical calculations and numerical simulations.

OCIS codes: (160.3918) Metamaterials; (240.0310) Thin films; (160.4760) Optical properties.

http://dx.doi.org/10.1364/OPTICA.3.000592

1. INTRODUCTION

Unlike a normal lens, which creates an image using a curved surface, a flat lens relies on negative refraction inside the material [1]. To obtain a diffraction-limited image, it is essential that the refracted angle inside the lens be exactly opposite the incident angle, for all incident angles. Hyperbolic metamaterials (HMMs) have been used to demonstrate negative refraction [2–7]. The effective permittivity of these metamaterials is anisotropic for TM-polarized light, with a tangential and longitudinal permittivity of opposite sign. This anisotropy leads to a hyperbolic dispersion relation describing light propagation through the metamaterial, which enables negative refraction of energy.

Figure 1(a) shows the calculated wave vector diagram $k_z(k_x)$ for a HMM composed of a periodic Ag/TiO_2 multilayer stack with very thin layers and a free-space wavelength $\lambda_0 = 364$ nm (red), obtained from effective medium theory (see "Effective medium theory" in Supplement 1). The inset shows a sketch of the multilayer geometry. We take typical values for the permittivity of Ag ($\varepsilon_m = -1.762 + 0.269i$) and TiO_2 ($\varepsilon_d = 7.270 + 0.163i$), and set the metal filling fraction to 75%. Initially, we assume the materials to be lossless so we neglect the imaginary parts of the dielectric constants. Next, the Bloch wave vector k_{Bl} for the multilayer structure is determined as a function of parallel wave vector momentum k_x using transfer matrix calculations (green) with unit cell size $a = d_m + d_d = 1$ nm. The isofrequency contour (IFC) plot shows very good correspondence with that of effective medium theory. The arrows drawn in Fig. 1(a) indicate the constructed refraction using this wave vector diagram for light incident from air on a semi-infinite region of this HMM geometry, under an angle of incidence of 30° with respect to the surface normal. As parallel wave vector momentum is conserved, the intersection of the dashed line in Fig. 1(a) with the IFC gives the refracted wave vector k_{refr} (red). The orientation of the Poynting vector S_{refr} (purple) is given by the derivative $\partial\omega/\partial k$, which is normal to the tangent at this point. The direction is determined by calculating the wave vector diagram for different λ_0 (not shown). The Poynting vector is oriented in the negative x direction, with a refraction angle of −7°, indicating negative refraction of energy.

The calculated refraction angle as a function of angle of incidence for the HMM is shown in Fig. 1(b) (red line). For comparison, the ideal case required for flat lensing—given by $\theta_{\mathrm{refr}} = -\theta_{\mathrm{inc}}$—is also shown as a black dashed line. The angular response for the HMM strongly deviates from this ideal case. This makes a HMM design unsuitable for realizing a flat lens as it would exhibit strong aberrations, leading to a poorly defined focus [8–10].

This problem is fundamentally caused by the hyperbolic shape of the IFC. To achieve the ideal negative refraction, a spherical IFC would be required, leading to an isotropic, angle-independent response. Therefore, we investigate the effect of increased unit cell size on the shape of the IFC. For example, the IFC for a HMM in which the unit cell size is increased to $a = 50$ nm strongly deviates from the effective medium result [blue line in Fig. 1(a)]. This is due to spatial dispersion, where the effective permittivity now depends on the incident wave vector [11–13].

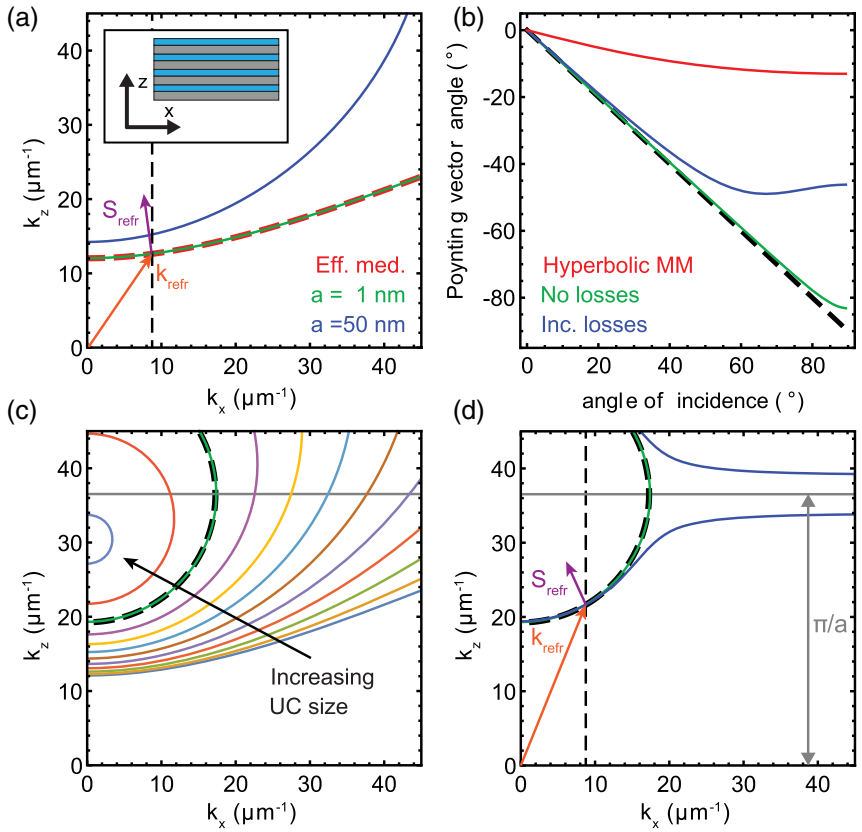

Fig. 1. (a) Hyperbolic IFC calculated for $\lambda_0 = 364$ nm ($k_0 = 17.3$ μm^{-1}) described by effective medium theory (red) and a periodic Ag/TiO_2 multilayer structure with a 1 nm unit cell (green), with $d_m = 3d_d$ and neglecting losses. Increasing the unit cell size to 50 nm bends the IFC away from the hyperbole (blue). The vertical dashed line corresponds to the parallel momentum of a plane wave in air incident at 30°. The Poynting vector shows negative refraction. The inset shows a sketch of the geometry, where gray corresponds to Ag and blue to TiO_2. (b) Calculated Poynting vector angle for the hyperbolic metamaterial (red), ideal spherical IFC (green), and realistic geometry including losses (blue). The black dashed line corresponds to the ideal case $\theta_{refr} = -\theta_{inc}$. (c) Increasing the unit cell size from $a = 1$ nm to $a = 100$ nm changes the curvature of the IFC. For a unit cell size of $a = 86.0$ nm, with $d_m = 64.6$ nm and $d_d = 21.4$ nm, the curvature is spherical with a radius equal to k_0 (black dashed curve). The gray line corresponds to the band edge, located at $k_z = \pi/a$. (d) Including losses, the IFC changes shape [blue, green is lossless from (c)], but the curvature is the same up to large angles of incidence (55°).

The strength of this effect is determined by the ratio of the thickness of the layers to the wavelength. Figure 1(c) shows how the IFC changes as the unit cell size is gradually increased from 1 to 100 nm, while keeping the ratio of metal and dielectric layer thickness fixed. The shape of the IFC shows a transition from hyperbolic to spherical, centered around the band edge, $k_z = \pi/a$. Interestingly, if the layer thicknesses and material permittivity are chosen correctly, the curvature of the IFC can be matched with that of free space, defined as a circle with radius $k_0 = 2\pi/\lambda_0$ (black dashed line). For $\lambda_0 = 364$ nm and for TM-polarization, the IFC is found to be spherical for $a = 86.0$ nm, with $d_m = 64.6$ nm and $d_d = 21.4$ nm (see "Design optimization" in Supplement 1 for the optimization). The spherical IFC implies that, for all incident angles, energy will be refracted with a negative angle equal in magnitude to the positive angle of incidence [14]. The green line in Fig. 1(b) shows the calculated angular response of the Poynting vector for the optimum geometry. The result is very close to the ideal curve up to very large angles of incidence. Note that so far we have determined the Poynting vector angle based on the IFC. In Supplement 1 section "Poynting vector angle," we compare this method to an analytical expression of a quasi-plane wave incident on a finite multilayer structure and observe good agreement for a multilayer structure consisting of five or more unit cells. For TE polarization, light undergoes positive refraction, and therefore the metamaterial only acts as a flat lens for TM-polarized light.

The IFC of this metamaterial design is fundamentally different from that of a coupled waveguide design [15,16], for which the IFC of the fundamental harmonic is spherical. Unlike the coupled waveguide design, here the IFC is centered around the band edge rather than the origin of the wave vector diagram. As a result, no guided modes propagate along the metal–dielectric interfaces, which form a loss channel for sources placed in the near field of the flat lens. In our single-periodic design, there can be a π phase difference between object and image (see "Phase condition" section in Supplement 1), depending on the number of unit cells. The interference between different harmonics of the Bloch wave is constructive for all angles [17]. It should be noted that a similar multilayer geometry was considered earlier [14,18] but was only explored theoretically. In the second reference, the IFC was also designed to be spherical, but with a radius of curvature larger than that of free space. This allows for the propagation of evanescent waves but also gives rise to aberrations and only a partial focus.

These calculations were performed for lossless materials. Next, we consider realistic material losses, taking into account the complex permittivity of Ag and TiO_2. Figure 1(d) shows the IFCs of

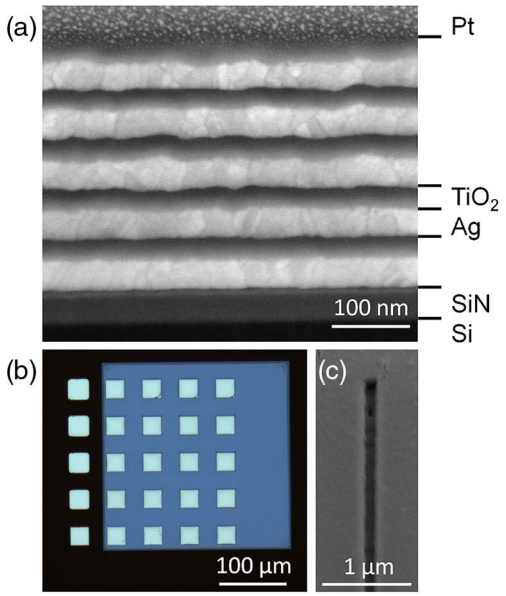

Fig. 2. (a) SEM image of a cross section of a fabricated multilayer structure. Five unit cells of Ag (light) and TiO_2 (dark) are clearly visible. The top TiO_2 layer is overcoated by Pt to improve the quality of the FIB cross-section. (b) Optical microscope image of multilayer structures (25×25 µm) deposited on a SiN membrane window (blue). The other regions of the multilayer stack are removed using a lift-off procedure. The opposite side of the membrane window is coated with a Cr masking layer, in which slits acting as an object for the flat lens are fabricated using FIB milling. (c) SEM image of a 100 nm wide slit in the Cr masking layer. The underlying SiN is exposed.

our optimized geometry, including losses (blue). The lossless case is also plotted for reference (green). The IFC is nearly spherical for $k_x < 14$ µm^{-1}, corresponding to an angle of incidence of ~55°. At larger angles, the IFC deviates significantly from the spherical shape. In this wave vector regime, most of the field is localized in the metal layers, which are absorbing. The calculated angular response of the Poynting vector for this geometry is shown in Fig. 1(b) (blue). Indeed, it is very close to the ideal curve (black dashed) for angles of incidence below 55°, corresponding to an effective numerical aperture (NA) of 0.8. We find that increased material losses effectively reduce the NA of the flat lens (see "Impact of loss on NA" section in Supplement 1).

2. EXPERIMENTAL OBSERVATION OF A FLAT LENS

To demonstrate the focusing properties of the single-periodic metamaterial flat lens experimentally, we fabricate an Ag/TiO_2 metal/dielectric multilayer stack using physical vapor deposition, as is described in the Methods section of the Supplement 1. A cross section of the multilayer stack is shown in Fig. 2(a). The multilayer stack is deposited on a 50 nm SiN membrane, and parts of the stack are removed using a lift-off process [Fig. 2(b)] to allow for accurate reference measurements on the same sample. The back side of the SiN is covered by an opaque 150 nm thick Cr film, through which slits are milled using focused ion beam milling [see Fig. 2(c)]. We use these slits as the objects to be imaged by the flat lens.

The multilayer structure consists of five unit cells with $d_m = 53.2$ nm and $d_d = 25.0$ nm, which are slightly different than

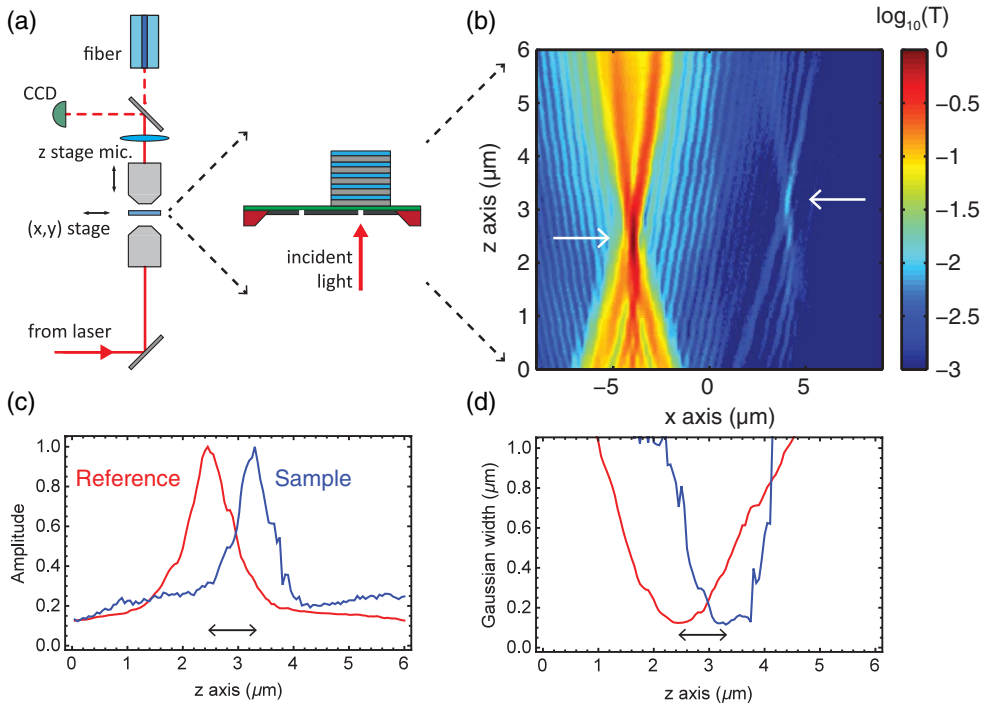

Fig. 3. (a) Sketch of the confocal microscope setup. The TM-polarized incident beam is weakly focused on the object slit. The sample stage is scanned in the lateral x direction. The top collection arm of the microscope body is scanned in the vertical z direction. (b) Confocal scan ($\lambda_0 = 364$ nm) of the signal of a reference slit (left) and sample slit (right) above the multilayer metamaterial. The normalized transmitted signal is plotted on a $\log_{10}$ scale. There is a large difference in amplitude between reference and sample due to the reflection and absorption by the multilayer stack. Focus positions are indicated by the white arrows. Normalized amplitude (c) and width (d) of the fitted Gaussian profile as a function of z. A clear vertical offset of 790 nm (indicated by the black arrow) is observed between the reference (red) and sample (blue) signal; the corresponding distance between lens surface and focus is 350 nm.

those considered in the calculations just shown in order to correct for the experimentally obtained optical constants of the deposited layers. The total lens thickness is $L = 390$ nm, and the distance from the object to the lens is $d_s = 50$ nm (the SiN membrane thickness). Therefore, we expect a lens–image separation of $d_i = 340$ nm based on the geometrical construction with negative refraction; $L = d_s + d_i$. We use a Witec α300SR confocal microscope to weakly focus TM-polarized $\lambda_0 = 364$ nm light from an Ar ion laser on the object slit (see Fig. 3). The transmitted light is collected using a 100 × objective (Zeiss Epiplan-NEOFLUAR 100 × /0.9 NA), focused onto a collection fiber (25 μm core diameter), and sent to a spectrometer. The lateral resolution is approximately 200 nm at $\lambda_0 = 364$ nm. The sample is scanned through the focus of the microscope using a piezoelectric stage in the x-direction, normal to the slit. The upper microscope body is scanned in height, to measure the vertical dependence of the image plane.

First, we scan the sample laterally such that two object slits are moved through the optical axis of the microscope—one covered by the multilayer flat lens, the other a reference slit [Fig. 3(a)]. The reference slit will only show a focus when the object slit itself is in the focus of the collection objective. Light transmitted through the flat lens will be focused just above the flat lens, and we can compare the focal point with that of the reference object slit. Figure 3(b) shows the result of the scan. Light from the reference slit is much more intense as it is directly transmitted (left), whereas the light from the slit underneath the lens is partially reflected and absorbed in the metamaterial (right). The spatial intensity distribution along x is analyzed by taking cross cuts through the data at a fixed height z. A Gaussian profile is fitted to the recorded signal, which is a good approximation to the focus shape near the focal position. Figures 3(c) and 3(d) show the normalized fitted amplitude and Gaussian width of both the reference (red) and the sample (blue) signal. The maximum amplitude and minimum width correspond to the same position for both the reference and the sample, which we take as the focal position. We find that the focus formed by the flat lens is positioned 790 nm away from the object, which is 350 nm above the top lens interface. This agrees very well with the expected lens–image separation of 340 nm, calculated using $L = d_s + d_i$.

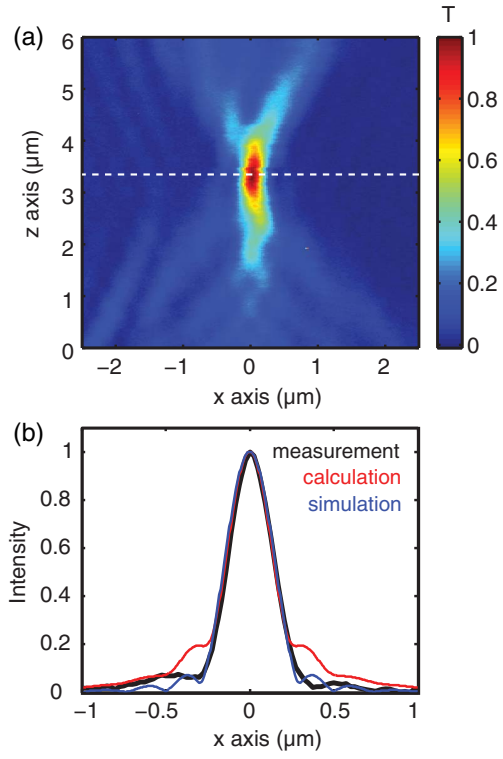

Fig. 4. (a) Confocal scan ($\lambda_0 = 364$ nm) shows the normalized transmission as a function of lateral sample position x and vertical microscope body position z. A clear image of the slit is observed with a FWHM of 350 nm. (b) Measured spatial intensity profile through the focus (black), compared to dipole calculations (red) and a FDTD simulation of the complete structure (blue).

To study the spatial characteristics of the focus in more detail, we perform a high-resolution scan of a single slit underneath the flat lens. Figure 4(a) shows the focus above the surface of the lens. A cross cut through the focus is shown in Fig. 4(b) (black). The minimum full width at half-maximum (FWHM) is found to be ≈350 nm. We compare this with the calculated image formed of a horizontal dipole placed below the flat lens using the Green's tensor in a multilayer structure (red) [19], and find a very similar FWHM. Lumerical finite-difference-time-domain (FDTD) simulations are also performed for the geometry, and the cross cut of the image found (blue) also agrees very well with the experimental result. Furthermore, with these FDTD simulations, we have investigated the influence of slit width on the focus and observe no significant change in the FWHM for a slit width less than 200 nm. The experiment was performed at a single wavelength. In the "Chromatic aberration" section of the Supplement 1, we numerically quantify the chromatic aberrations of the lens: by changing the emission wavelength by ±5 nm, we find a focal length shift of approximately ∓100 nm and an increase of the FWHM of 5%. Overall, these results demonstrate that a metal–dielectric multilayer structure indeed acts as a flat lens.

3. CONCLUSION

In conclusion, we realized a single-periodic planar multilayer geometry that acts as a flat lens starting from a hyperbolic metamaterial design formed by a Ag/TiO_2 multilayer stack with a very small unit cell size. We gradually increase the unit cell size far above the effective medium approximation limit to shape the angular response. Using properly chosen layer thicknesses, the isofrequency contour can be designed to be spherical in shape, with a radius equal to that of the contour in free space. This geometry shows all-angle negative refraction, and can therefore act as a flat lens. An optimized flat lens geometry based on a Ag/TiO_2 multilayer stack, with layer thicknesses $d_m = 53.2$ nm and $d_d = 25.0$ nm, is fabricated using physical vapor deposition. We use confocal microscopy at $\lambda_0 = 364$ nm to study the spatial shape of the image formed above the flat lens. A clear focus is resolved with a full-width half-maximum of 350 nm, in agreement with calculations and simulations. We find that the image is positioned 350 nm from the lens surface, as expected from theory. Such a short focal length is a unique feature of the flat lens and enables many applications that cannot be achieved with conventional macroscopic lens designs. For example, the flat lens may find applications in optical recording systems where the distance between write head and recording medium is in the nanoscale range, or in nanofluidic sensors where the lens can form an integral part of the device. Additionally, because the multilayer structure is easy to fabricate and is translation symmetric, a very

large area sample can be covered with the flat lens. Due to the absence of an optical axis, such a flat lens then enables large-scale parallel imaging.

Funding. Foundation for Fundamental Research on Matter (FOM); Nederlandse Organisatie voor Wetenschappelijk Onderzoek (NWO); European Research Council (ERC).

See Supplement 1 for supporting content.

REFERENCES

1. V. G. Veselago, "The electrodynamics of substances with simultaneously negative values of epsilon and mu," Sov. Phys. Usp. **10**, 509–514 (1968).
2. P. Belov, "Backward waves and negative refraction in uniaxial dielectrics with negative dielectric permittivity along the anisotropy axis," Microwave Opt. Technol. Lett. **37**, 259–263 (2003).
3. D. R. Smith, P. Kolinko, and D. Schurig, "Negative refraction in indefinite media," J. Opt. Soc. Am. B **21**, 1032–1043 (2004).
4. A. J. Hoffman, L. Alekseyev, S. S. Howard, K. J. Franz, D. Wasserman, V. A. Podolskiy, E. E. Narimanov, D. L. Sivco, and C. Gmachl, "Negative refraction in semiconductor metamaterials," Nat. Mater. **6**, 946–950 (2007).
5. J. Yao, Z. Liu, Y. Liu, Y. Wang, C. Sun, G. Bartal, A. M. Stacy, and X. Zhang, "Optical negative refraction in bulk metamaterials of nanowires," Science **321**, 930 (2008).
6. A. Poddubny, I. Iorsh, P. Belov, and Y. Kivshar, "Hyperbolic metamaterials," Nat. Photonics **7**, 948–957 (2013).
7. C. Argyropoulos, N. M. Estakhri, F. Monticone, and A. Alù, "Negative refraction, gain and nonlinear effects in hyperbolic metamaterials," Opt. Express **21**, 15037–15047 (2013).
8. D. R. Smith, D. Schurig, M. Rosenbluth, S. Schultz, S. A. Ramakrishna, and J. B. Pendry, "Limitations on subdiffraction imaging with a negative refractive index slab," Appl. Phys. Lett. **82**, 1506–1508 (2003).
9. D. R. Smith, D. Schurig, J. J. Mock, P. Kolinko, and P. Rye, "Partial focusing of radiation by a slab of indefinite media," Appl. Phys. Lett. **84**, 2244–2246 (2004).
10. H. Liu, Q. Lv, H. Luo, S. Wen, W. Shu, and D. Fan, "Focusing of vectorial fields by a slab of indefinite media," J. Opt. A **11**, 105103 (2009).
11. A. A. Orlov, P. M. Voroshilov, P. A. Belov, and Y. S. Kivshar, "Engineered optical nonlocality in nanostructured metamaterials," Phys. Rev. B **84**, 045424 (2011).
12. A. V. Chebykin, A. A. Orlov, A. V. Vozianova, S. I. Maslovski, Y. S. Kivshar, and P. A. Belov, "Nonlocal effective medium model for multilayered metal-dielectric metamaterials," Phys. Rev. B **84**, 115438 (2011).
13. A. V. Chebykin, A. A. Orlov, C. R. Simovski, Y. S. Kivshar, and P. A. Belov, "Nonlocal effective parameters of multilayered metal-dielectric metamaterials," Phys. Rev. B **86**, 115420 (2012).
14. J. Zhang, H. Jiang, B. Gralak, S. Enoch, G. Tayeb, and M. Lequime, "Towards-1 effective index with one-dimensional metal-dielectric metamaterial: a quantitative analysis of the role of absorption losses," Opt. Express **15**, 7720–7729 (2007).
15. E. Verhagen, R. de Waele, L. Kuipers, and A. Polman, "Three-dimensional negative index of refraction at optical frequencies by coupling plasmonic waveguides," Phys. Rev. Lett. **105**, 223901 (2010).
16. T. Xu, A. Agrawal, M. Abashin, K. J. Chau, and H. J. Lezec, "All-angle negative refraction and active flat lensing of ultraviolet light," Nature **497**, 470–474 (2013).
17. R. Maas, E. Verhagen, J. Parsons, and A. Polman, "Negative refractive index and higher-order harmonics in layered metallodielectric optical metamaterials," ACS Photon. **1**, 670–676 (2014).
18. H. Shin and S. Fan, "All-angle negative refraction and evanescent wave amplification using one-dimensional metallodielectric photonic crystals," Appl. Phys. Lett. **89**, 151102 (2006).
19. M. Paulus, P. Gay-Balmaz, and O. J. F. Martin, "Accurate and efficient computation of the Green's tensor for stratified media," Phys. Rev. E **62**, 5797–5807 (2000).